Chemical
Science

ROYAL SOCIETY
OF CHEMISTRY

EDGE ARTICLE

View Article Online
View Journal | View Issue

Cite this: *Chem. Sci.*, 2025, **16**, 21423

Near-unity and narrow green emission from a manganese(II) bromide for efficient WLEDs and 3D X-ray imaging

Mengzhu Wang, Xiaolong Li, Siwen Zou, Haixia Cui, Yongjing Deng, Jiangang Li, Yi Jiang, Longlu Wang, Shujuan Liu, Qiang Zhao * and Yun Ma *

Received 26th June 2025
Accepted 13th October 2025

DOI: 10.1039/d5sc04721h

rsc.li/chemical-science

Developing efficient, narrow-band, and environmentally friendly emitters is crucial for advanced optoelectronics. Herein, we report a zero-dimensional (0D) organic–inorganic hybrid manganese(II) halide, $(TPS)_2MnBr_4$ (TPS = triphenylsulfonium), engineered *via* cation selection. This material simultaneously achieves near-unity photoluminescence quantum yield (PLQY ≈ 99.6%) and exceptionally narrow green emission (FWHM = 40 nm) for a Mn^{2+} emitter. Structural analysis and theoretical calculations reveal that the rigid TPS^+ cation induces a specific crystal packing that minimizes $[MnBr_4]^{2-}$ tetrahedral distortion through weaker hydrogen bonding interactions. This structural optimization leads to suppressed electron–phonon coupling, explaining the narrow bandwidth while maintaining high efficiency. These outstanding properties enable high-performance white light-emitting diodes (WLEDs) and 3D X-ray Imaging. This work demonstrated targeted cation engineering as a powerful strategy to overcome intrinsic Mn^{2+} limitations and presents a high-performance, eco-friendly material for multifunctional optoelectronic applications.

Introduction

Zero-dimensional (0D) organic–inorganic hybrid metal halides (OIMHs) offer a versatile platform for optoelectronics, providing tunable structures while circumventing the toxicity and stability issues of lead-based perovskites.[1–5] Within this class, lead-free manganese(II) halides, featuring $[MnX_4]^{2-}$ (X= Cl or Br or I) tetrahedra, are highly attractive due to their earth abundance, low cost, low toxicity, and characteristic bright green emission suitable for RGB displays.[6–15] This emission stems from the spin-forbidden $^4T_1(G) \rightarrow {}^6A_1(S)$ d–d transition.[16–21] However, Mn^{2+} emitters face a significant intrinsic challenge: strong electron–phonon coupling inherent to this transition promotes non-radiative decay,[22] limiting photoluminescence quantum yields (PLQY), and broadens the emission bandwidth (FWHM), typically to the 45–75 nm range. This presents a major obstacle, as achieving the ideal combination of near-perfect PLQY for maximum brightness and narrow FWHM for exceptional color purity is paramount for advancing many optoelectronic technologies, but is fundamentally difficult due to these Mn^{2+} photophysics. Therefore, developing strategies to attain this synergy within stable, cost-effective, and environmentally benign Mn(II) halide frameworks remains a primary objective.

Recently, significant research efforts focus on overcoming these Mn^{2+} limitations through structural engineering, primarily by employing bulky organic cations to isolate the $[MnX_4]^{2-}$ units.[23] This isolation effectively increases Mn–Mn distances, suppressing quenching mechanisms and enabling high PLQYs in many systems.[24–31] However, simultaneously reducing the FWHM requires more subtle control over the Mn^{2+} local environment. For example, Lin *et al.* have demonstrated the FWHM of tetrahedral Mn(II) emission is highly sensitive to the degree of structural distortion within the $[MnX_4]^{2-}$ unit and the strength of hydrogen bonding interactions between the cation and the anion.[32] Specifically, weaker hydrogen bonds and reduced tetrahedral distortion were correlated with narrower FWHM. Concurrently, preserving high PLQY requires careful consideration of the electronic structure. Work by Fu *et al.* highlighted that the band alignment between the organic cation matrix and the Mn(II) halide unit, particularly in the excited state, dictates whether photogenerated excitons remain confined within the Mn(II) center or transfer to the organic matrix.[33] This implies that the choice of organic cation is critical not only for structural isolation and FWHM modulation but also for maintaining efficient radiative recombination pathways.

This intricate interplay between structural factors (distortion, H-bonding, rigidity) influencing FWHM and electronic factors governing PLQY necessitates a holistic design strategy.

State Key Laboratory of Flexible Electronics (LoFE), Jiangsu Key Laboratory of Smart Biomaterials and Theranostic Technology, Institute of Advanced Materials (IAM), College of Electronic and Optical Engineering, College of Flexible Electronics (Future Technology), Nanjing University of Posts and Telecommunications (NUPT), 9 Wenyuan Road, Nanjing 210023, Jiangsu, China. E-mail: iamqzhao@njupt.edu.cn; iamyma@njupt.edu.cn

We hypothesized that employing a specific organic cation possessing both significant steric bulk and high conformational rigidity could synergistically address both challenges. We selected the triphenylsulfonium (TPS^+) cation, anticipating that its bulkiness would ensure effective isolation of $[MnBr_4]^{2-}$ units for high intrinsic PLQY, while its defined, rigid structure could impose a unique and highly ordered crystal packing. This specific packing environment, we posited, might lead to minimal tetrahedral distortion and potentially weaker/optimized hydrogen bonding, thereby reducing electron–phonon coupling to achieve a narrowed FWHM, while simultaneously ensuring favorable excited-state band alignment to preserve the near-unity PLQY.

Herein, we demonstrate the success of this targeted cation engineering strategy through the synthesis and comprehensive characterization of a novel 0D manganese bromide hybrid, $(TPS)_2MnBr_4$. This material achieves the highly sought-after combination of a near-unity PLQY (∼99.6%) and a substantially narrowed green emission band with FWHM = 40 nm, representing a significant step towards ideal green emitters based on Mn^{2+}. We systematically investigate the structure–property relationships, correlating the crystallographic features and cation–anion interactions with the observed reduced electron–phonon coupling. Critically, we demonstrate the practical impact of these exceptional properties by fabricating high-performance devices for wide-color-gamut WLEDs and high-resolution X-ray imaging. This work provides not only a benchmark material but also suggests a rational design pathway for developing next-generation, high-performance, lead-free manganese halide emitters for multifunctional optoelectronic applications.

Results and discussion

Synthesis and characterization

Guided by the strategy employing the TPS^+ cation to achieve specific structural and photophysical properties, we successfully synthesized high-quality single crystals of the target 0D manganese(II) halide hybrids $(TPS)_2MnBr_4$ and its chloride analogue $(TPS)_2MnCl_4$. The latter serves as a crucial reference compound to elucidate the impact of the halide anion and associated structural changes.[34] Both materials were prepared using a facile solvent-antisolvent recrystallization method at room temperature, starting from stoichiometric amounts of the respective triphenylsulfonium halide (TPSX) and manganese(II) halide hydrate ($MnBr_2\cdot 4H_2O$, 98%) precursors dissolved in ethanol, with ethyl acetate acting as the antisolvent (Fig. S1).

The bulk phase purity and crystallinity of the as-synthesized materials were confirmed by powder X-ray diffraction (PXRD). As shown later (Fig. 1c and f), the experimental PXRD patterns for both $(TPS)_2MnCl_4$ and $(TPS)_2MnBr_4$ powders exhibit sharp diffraction peaks that match excellently with the patterns simulated from their respective single-crystal X-ray diffraction (SCXRD) data. We have carried out rietveld refinements of the powder XRD data for both $(TPS)_2MnCl_4$ and $(TPS)_2MnBr_4$, and the results are now provided in the Fig. S2 and S3. For $(TPS)_2MnCl_4$, the refinement yielded $R_p = 7.01\%$, $R_{wp} = 9.21\%$, and GoF = 1.72. In addition, for $(TPS)_2MnBr_4$, the refinement gave $R_p = 6.68\%$, $R_{wp} = 8.59\%$, and GoF = 1.65. These refinement parameters are well within acceptable ranges, confirming the high crystallinity and structural reliability of our samples. This agreement verifies the successful formation of the target crystalline phases and their consistency between single crystals and bulk powder samples. The fundamental structural framework, determined by SCXRD and discussed next, features isolated $[MnX_4]^{2-}$ tetrahedra effectively separated by the bulky TPS^+ cations, fulfilling the primary design criterion for suppressing Mn–Mn interactions. The thermogravimetry analysis (TGA) curve, presented in Fig. S4, reveals that $(TPS)_2MnBr_4$ is highly stable upon heating. The onset of thermal decomposition occurs at a high temperature of approximately 340 °C, indicating its good thermal stability.

Crystal structure and photophysical properties

Detailed structural insights were obtained *via* single-crystal X-ray diffraction (SCXRD) analysis for both $(TPS)_2MnCl_4$ and $(TPS)_2MnBr_4$. $(TPS)_2MnCl_4$ crystallizes in the lower-symmetry monoclinic $P12_1/n$ space group (Fig. 1b). The structure definitively confirms the targeted 0D arrangement, where individual $[MnCl_4]^{2-}$ tetrahedral anions are effectively isolated from each other by the large, sterically demanding triphenylsulfonium cations. The shortest Mn⋯Mn distance is 9.290 Å (Fig. S5a), validating our strategy of using bulky cations to suppress interunit interactions, which is crucial for achieving high PLQY. Within the asymmetric unit, there are two crystallographically distinct Mn sites. The $[MnCl_4]^{2-}$ tetrahedra associated with these sites exhibit notable distortion from ideal T_d symmetry: Mn–Cl bond lengths span from 2.346(7) Å to 2.373(5) Å, and the Cl–Mn–Cl bond angles deviate significantly, ranging from 104.57(2)° to 113.15(2)°. Crystallographic data of $(TPS)_2MnCl_4$ and $(TPS)_2MnBr_4$ were listed in Table S1. This degree of distortion will be quantified later and correlated with the photophysical properties.

In contrast, $(TPS)_2MnBr_4$ adopts the higher-symmetry rhombohedral *R*-3*c* space group (Fig. 1e). This structure also maintains the 0D character with well-isolated $[MnBr_4]^{2-}$ tetrahedra (shortest Mn⋯Mn distance = 9.784 Å) (Fig. S5b). A key difference is the presence of only one unique crystallographic Mn site in the bromide structure, suggesting a more uniform environment for the Mn^{2+} emitters compared to the chloride analogue. The $[MnBr_4]^{2-}$ tetrahedra feature Mn–Br bond lengths of 2.474 Å and 2.514 Å, and Br–Mn–Br angles varying between 105.19° and 113.39°. Qualitatively, the range of bond angles suggests a distortion, but critically, as will be shown through quantitative analysis, the $[MnBr_4]^{2-}$ units in this structure exhibit significantly less distortion compared to the $[MnCl_4]^{2-}$ units. This reduced distortion, influenced by the interplay between the TPS^+ cation, the larger Br^- anion, and the resulting crystal packing and hydrogen bonding network is hypothesized to be directly responsible for the anticipated narrowing of the emission bandwidth, aligning with recent findings in related Mn(II) halide systems.[32,35]

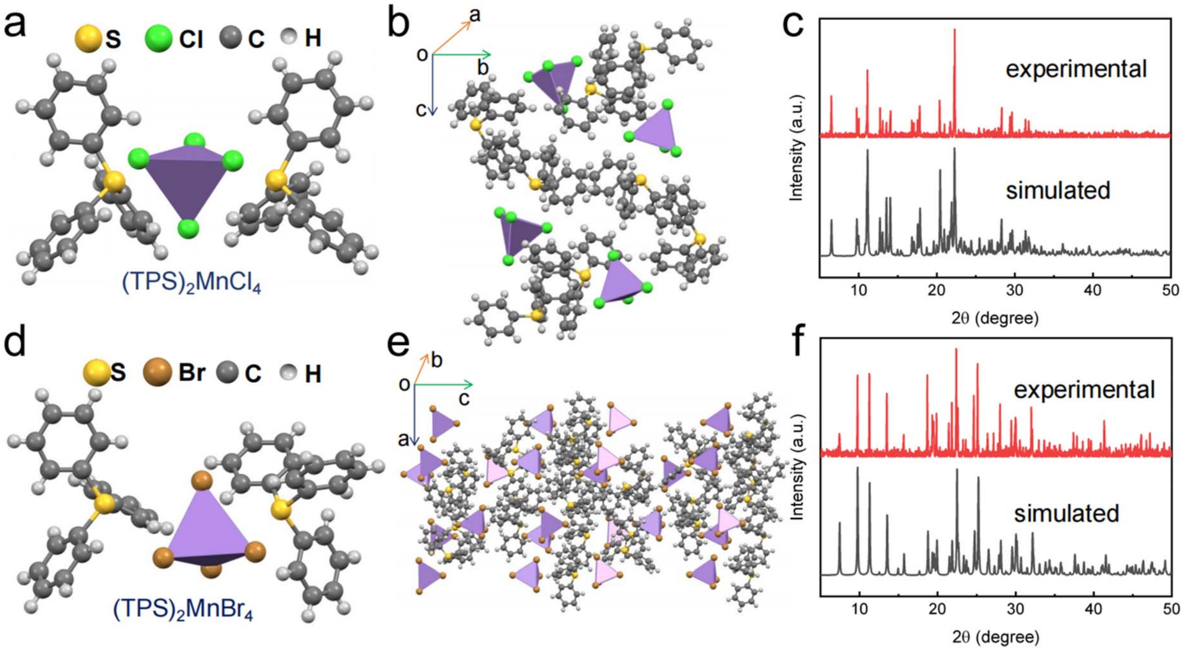

Fig. 1 (a) View highlighting the coordination environment of the $[MnCl_4]^{2-}$ anion (purple polyhedron) with neighboring TPS^+ cations in $(TPS)_2MnCl_4$. (b) Crystal packing diagram showing the arrangement within the unit cell of $(TPS)_2MnCl_4$. (c) Comparison of experimental (red trace) and simulated (black trace) PXRD patterns for $(TPS)_2MnCl_4$. (d) Analogous view showing the coordination environment of the $[MnBr_4]^{2-}$ anion in $(TPS)_2MnBr_4$. (e) Crystal packing diagram for $(TPS)_2MnBr_4$. (f) Comparison of experimental (red trace) and simulated (black trace) PXRD patterns for $(TPS)_2MnBr_4$.

The steady-state photoluminescence (PL) and excitation (PLE) spectra of $(TPS)_2MnCl_4$ and $(TPS)_2MnBr_4$ were investigated at room temperature to evaluate their fundamental optical properties (Fig. 2a and d). Both compounds display characteristic excitation profiles consistent with tetrahedrally coordinated Mn^{2+}. Broad absorption bands span the UV-blue region (~280–500 nm). Absorption below ~350 nm likely involves contributions from the π–π* transitions of the TPS^+

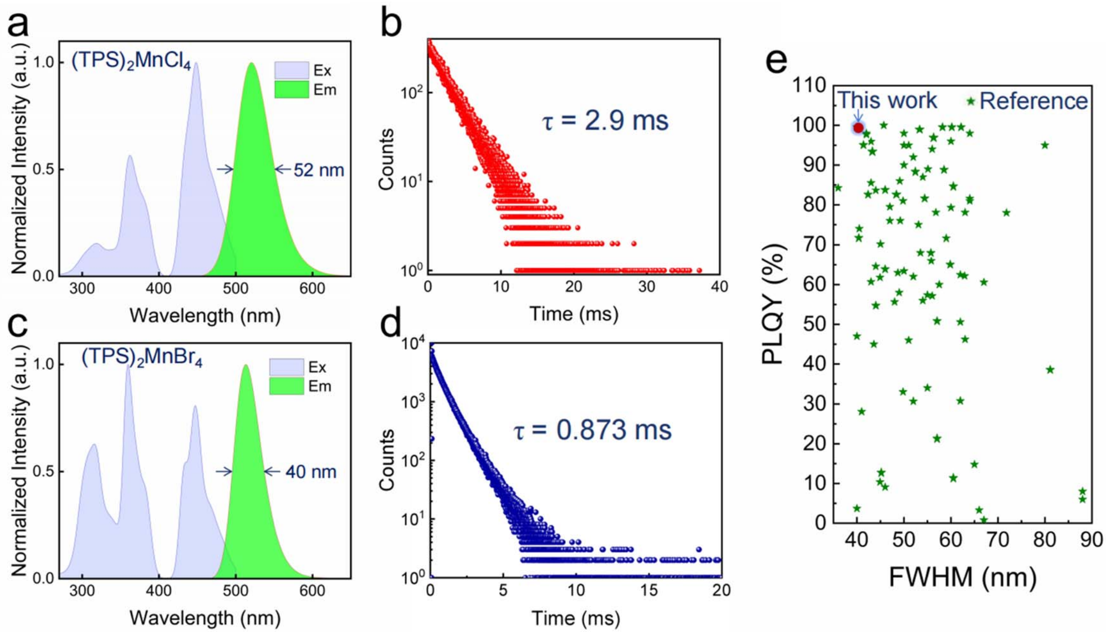

Fig. 2 Room temperature PL excitation (PLE, blue shaded area) and emission (PL, green shaded area) spectra for (a) $(TPS)_2MnCl_4$ and (c) $(TPS)_2MnBr_4$. Photoluminescence decay curves for (b) $(TPS)_2MnCl_4$ and (d) $(TPS)_2MnBr_4$. (e) PLQY and FWHM performance distribution of Green emitting manganese(II) halide.

cations, potentially facilitating energy transfer to the Mn^{2+} centers. More importantly, distinct peaks between ~350 nm and 500 nm correspond to the parity- and spin-forbidden d–d electronic transitions of Mn^{2+} from the $^6A_1(S)$ ground state to various excited states (including assignments like $^6A_1(S) \rightarrow {}^4E(D)$, $^4T_2(D)$, $^4A_1/^4E(G)$, $^4T_2(G)$, $^4T_1(G)$).[36,37] Upon excitation at 361 nm, both materials exhibit intense green emission characteristic of the $^4T_1(G) \rightarrow {}^6A_1(S)$ transition within the isolated $[MnX_4]^{2-}$ tetrahedra. $(TPS)_2MnCl_4$ emits with a peak maximum at 520 nm, displaying a Full-Width at Half-Maximum (FWHM) of 52 nm (approx. 0.236 eV). In striking contrast, $(TPS)_2MnBr_4$ emits slightly blue-shifted at $\lambda_{em} = 515$ nm, consistent with the weaker ligand field of Br^-, but crucially, its emission band is significantly narrower, with an FWHM of only 40 nm (approx. 0.186 eV). This substantial ~25% reduction in FWHM for the bromide analogue is a key achievement and directly supports our hypothesis that the specific structural environment imposed by the TPS^+ cation in the bromide lattice effectively suppresses factors contributing to spectral broadening.

The effectiveness of the TPS^+ cation in isolating the Mn^{2+} emitters and minimizing non-radiative decay pathways is dramatically highlighted by the measured PLQY, obtained using an integrating sphere (Fig. S6). $(TPS)_2MnCl_4$ already exhibits a high PLQY of 92.0%. Remarkably, $(TPS)_2MnBr_4$ achieves a near-unity PLQY of 99.6%. The temperature dependence PLQY of $(TPS)_2MnBr_4$ is measured, as shown in Fig. S7. When the temperature ranges from 80 K to 340 K, the PLQY remains above 99.6%, proving the excellent luminescent performance at room temperature. We have systematically investigated the PLQY of $(TPS)_2MnBr_4$ as a function of the excitation power density over a wide range, from 10^{-3} to 10^2 W cm^{-2}, as shown in Fig. S8. The data reveals a clear dependence: at very low power densities (<10^{-2} mW cm^{-2}), the PLQY is moderately reduced. However, it rapidly rises with increasing power and then saturates at our reported near-unity value (~99.6%) across a broad range of moderate to high power densities (from ~0.1 mW cm^{-2} to 100 mW cm^{-2}). This behavior is a classic signature of the saturation of non-radiative recombination centers, such as trap states.[38] At low excitation fluences, these trap states effectively compete with the radiative pathway for a fraction of the photogenerated excitons, thus lowering the measured efficiency. However, as the excitation intensity increases, these limited non-radiative channels become saturated, allowing most excitons to decay through the highly efficient intrinsic radiative pathway of the Mn^{2+} centers. This confirms that the true intrinsic quantum efficiency of our material is indeed near-unity.These exceptionally high values confirm that the structural design successfully minimizes quenching processes, allowing the radiative decay from the $^4T_1(G)$ state to dominate.

Time-resolved photoluminescence (TRPL) decay measurements further probe the excited-state dynamics. Both compounds exhibit luminescence decays on the millisecond/sub-millisecond timescale, characteristic of the spin-forbidden nature of the $^4T_1(G) \rightarrow {}^6A_1(S)$ transition. The decay curve of $(TPS)_2MnCl_4$ is well described by single exponential function, while the decay curves of $(TPS)_2MnBr_4$ is well described by double exponential function (Fig. S9). The extracted lifetimes differ significantly: $\tau = 2.90$ ms for $(TPS)_2MnCl_4$ and $\tau = 0.873$ ms for $(TPS)_2MnBr_4$. The much shorter lifetime observed for the bromide is attributed to the heavy atom effect of bromine, which enhances spin–orbit coupling. This increased coupling partially relaxes the spin selection rule, leading to a significantly higher transition probability compared to the chloride. In addition, TRPL spectrum of $(TPS)_2MnBr_4$ is measured, as shown in Fig. S10. As the delay time increases from 0 to 10 ms, the emission wavelength of $(TPS)_2MnBr_4$ remains at 515 nm. Overall, while both TPS-based halides are highly efficient emitters due to excellent Mn^{2+} isolation, $(TPS)_2MnBr_4$ stands out by simultaneously achieving near-unity PLQY and a significantly narrowed emission bandwidth (40 nm FWHM), as shown in Fig. 2e and Table S2. This combination points towards a unique structural environment in the bromide that minimizes both non-radiative recombination and spectral broadening effects.

Mechanism study

To elucidate the origin of the significantly narrower emission bandwidth observed for $(TPS)_2MnBr_4$ compared to $(TPS)_2MnCl_4$, we investigated their photoluminescence behavior as a function of temperature from 80 K to 300 K (Fig S11). As expected for emission processes influenced by lattice vibrations, cooling leads to a marked increase in PL intensity and a significant narrowing of the emission band for both compounds. A slight red shift in the peak position is also observed upon cooling, typically associated with lattice contraction effects. The thermal broadening of the emission band is a direct consequence of electron–phonon coupling, the interaction between the electronic states of the Mn^{2+} emitter and the vibrational modes (phonons) of the surrounding lattice. The strength of this coupling directly influences the emission FWHM. We can quantify this interaction by analyzing the temperature dependence of the FWHM using the following standard model:[39]

$$\mathrm{FWHM} = 2.36\sqrt{S\hbar\omega_{\mathrm{phonon}}}\sqrt{\coth\frac{\hbar\omega_{\mathrm{phonon}}}{2k_{\mathrm{B}}T}}$$

where S is the dimensionless Huang–Rhys factor representing the average number of phonons emitted during optical transition, $\hbar\omega_{\mathrm{phonon}}$ is the energy of the effective phonon mode coupled to the electronic transition, k_B is the Boltzmann constant, and T is the absolute temperature.

We extracted the FWHM values (in eV) from the temperature-dependent spectra and plotted them against temperature (Fig. 2a). Fitting these experimental data with the equation above yielded the electron–phonon coupling parameters for both compounds. For $(TPS)_2MnCl_4$: $S = 2.67$, $\hbar\omega_{\mathrm{phonon}} = 32.3$ meV. For $(TPS)_2MnBr_4$: $S = 2.46$, $\hbar\omega_{\mathrm{phonon}} = 26.2$ meV. Importantly, the Huang–Rhys factor for $(TPS)_2MnBr_4$ is distinctly smaller than that for $(TPS)_2MnCl_4$. This lower S value provides direct quantitative evidence for weaker electron–phonon coupling in the $(TPS)_2MnBr_4$ lattice environment compared to its chloride counterpart. The effective phonon energy coupled to the transition is also slightly lower in the bromide. Therefore, this intrinsically weaker electron–phonon coupling in

$(TPS)_2MnBr_4$, as reflected by its lower S factor, is the fundamental physical reason why it exhibits a significantly narrower emission FWHM (40 nm *vs.* 52 nm) at room temperature and maintains a narrower profile across the entire temperature range studied. This finding strongly supports the hypothesis that the specific structural arrangement facilitated by the TPS^+ cation within the bromide lattice creates an environment less susceptible to vibrational broadening effects.

Having established that $(TPS)_2MnBr_4$ exhibits weaker electron–phonon coupling (lower S factor) than $(TPS)_2MnCl_4$, we now seek to correlate this difference with specific structural features, namely the distortion of the Mn(II) tetrahedra and the nature of intermolecular interactions. Recent studies on related 0D Mn(II) halides have suggested a strong link between reduced tetrahedral distortion, often influenced by hydrogen bonding strength, and narrower emission FWHM.[32] First, we quantitatively assessed the distortion of the Mn(II) coordination tetrahedra using the calculated bond length distortion index (λ_{tet}) and bond angle variance (δ_{tet}^2) based on the SCXRD data (Fig. S12), using the following equations:[40,41]

$$\lambda_{\text{tet}} = \frac{1}{4}\sum_{i}^{4}\left(\frac{l_i - \bar{l}}{\bar{l}}\right)^2$$

$$\delta_{\text{tet}}^2 = \frac{1}{5}\sum_{i}^{6}(\theta_i - 109.47^\circ)^2$$

where $\bar{l}$ is the average Mn–X (X= Cl or Br) bond length, l_i is the individual Mn–X bond length, and θ_i is the individual bond angle of the tetrahedron. These calculations confirmed that the $[MnBr_4]^{2-}$ tetrahedra in $(TPS)_2MnBr_4$ ($\lambda_{\text{tet}} = 1.25 \times 10^{-5}$, $\delta_{\text{tet}}^2 = 9.23$) possess a significantly lower degree of distortion compared to the $[MnCl_4]^{2-}$ units in $(TPS)_2MnCl_4$ ($\lambda_{\text{tet}} = 3.38 \times 10^{-5}$, $\delta_{\text{tet}}^2 = 10.30$). Fig. 3b and c represent the hydrogen bond interactions in $(TPS)_2MnCl_4$ and $(TPS)_2MnBr_4$ crystals, respectively. Obviously, the hydrogen bond interaction in $(TPS)_2MnBr_4$ (2.897–3.022 Å) is weaker than that in $(TPS)_2MnCl_4$ (2.680–2.944 Å). To further investigate the role of intermolecular interactions, particularly hydrogen bonding (H⋯X), which can influence tetrahedral distortion, we employed Hirshfeld surface analysis (Fig. 3d and g) and the associated 2D fingerprint plots (Fig. 3e and h). The Hirshfeld surfaces visually map close contacts, while the fingerprint plots provide a quantitative summary, plotting the distance to the nearest nucleus inside (d_i) *versus* outside (d_e) the surface. Comparing the fingerprint plots for H⋯X interactions reveals distinct differences. The sharp "spikes" corresponding to the shortest H⋯X contacts terminate at a significantly larger minimum d_i value for $(TPS)_2MnBr_4$ ($d_i \approx 1.75$ Å, Fig. 3e) compared to $(TPS)_2MnCl_4$ ($d_i \approx 1.56$ Å, Fig. 3b). Since larger d_i and d_e values correspond to longer contact distances, this indicates that the hydrogen bonding interactions between the TPS^+ cations and the $[MnBr_4]^{2-}$ anions are generally weaker and/or longer than those involving the $[MnCl_4]^{2-}$ anions.

Based on these findings, we propose a structure–property correlation that the weaker hydrogen bonding network in $(TPS)_2MnBr_4$ exerts less external constraint on the manganese tetrahedra, allowing them to adopt a less distorted geometry. This reduced structural distortion, along with the potentially altered lattice vibrational dynamics associated with the weaker H-bonds, likely leads to the observed weaker electron–phonon coupling (lower S factor). Consequently, the radiative transition is less broadened by vibrational coupling, resulting in the significantly narrower emission FWHM (40 nm) observed for $(TPS)_2MnBr_4$.

Furthermore, density functional theory (DFT) calculations were performed on $(TPS)_2MnBr_4$ to provide further context on its electronic structure (Fig. 3f and i). The calculated band structure yields an indirect band gap (E_g) of 2.12 eV. Analysis of the Density of States (DOS) reveals that the valence band maximum (VBM) is primarily composed of hybridized Mn 3d and Br 4p orbitals, while the conduction band minimum (CBM) originates mainly from the orbitals of the TPS^+ cations. The calculated band structure shows relatively flat bands near the VBM. This lack of dispersion is a direct consequence of the structural isolation of the $[MnBr_4]^{2-}$ units, confirming their highly localized electronic nature and validating the assignment of a 0D electronic dimensionality based on the crystal structure.[32] Meanwhile, we have determined the exciton binding energies (E_b) of both compounds by analyzing the temperature-dependent PL intensities. The Arrhenius fits yield $E_b = 54.0$ meV for $(TPS)_2MnCl_4$ and $E_b = 67.0$ meV for $(TPS)_2MnBr_4$ (Fig. S13 and S14). These relatively high binding energies indicate that the photo-excited states are well confined within the $[MnX_4]^{2-}$ tetrahedra, which is consistent with the 0D electronic dimensionality of our systems. This localization minimizes inter-unit electronic coupling, contributing to the confinement of excitations and supporting the high observed PLQY, consistent with principles established for achieving efficient emission in such systems.

WLED application

To demonstrate the practical utility derived from the exceptional photophysical properties of $(TPS)_2MnBr_4$, particularly its near-unity PLQY and narrow emission band, we fabricated and evaluated a white light-emitting diode (WLED) device. The device was constructed by encapsulating a mixture of the green-emitting $(TPS)_2MnBr_4$ powder and a commercial narrow-band red phosphor ($K_2SiF_6:Mn^{4+}$, KSF) onto a standard blue InGaN chip ($\lambda_{\text{em}} \approx 460$ nm), as depicted in the inset of Fig. 4a. Upon electrical driving (20 mA), the optimized WLED produced bright white light (Fig. 4a and f) with excellent performance metrics: a high luminous efficacy (LE) of 108 lm W^{-1}, a suitable correlated color temperature (CCT) of 6189 K for general lighting, and a good color rendering index (CRI) of 86. The CIE 1931 chromaticity coordinates were (0.32, 0.33), located well within the white region. The high LE achieved is a direct consequence of the near-unity internal quantum efficiency (PLQY ≈ 99.6%) of the $(TPS)_2MnBr_4$ green phosphor, which minimizes energy losses during the blue-to-green light conversion process. Most significantly for display applications, the narrow FWHM (40 nm) of the green emission from $(TPS)_2MnBr_4$ enables the

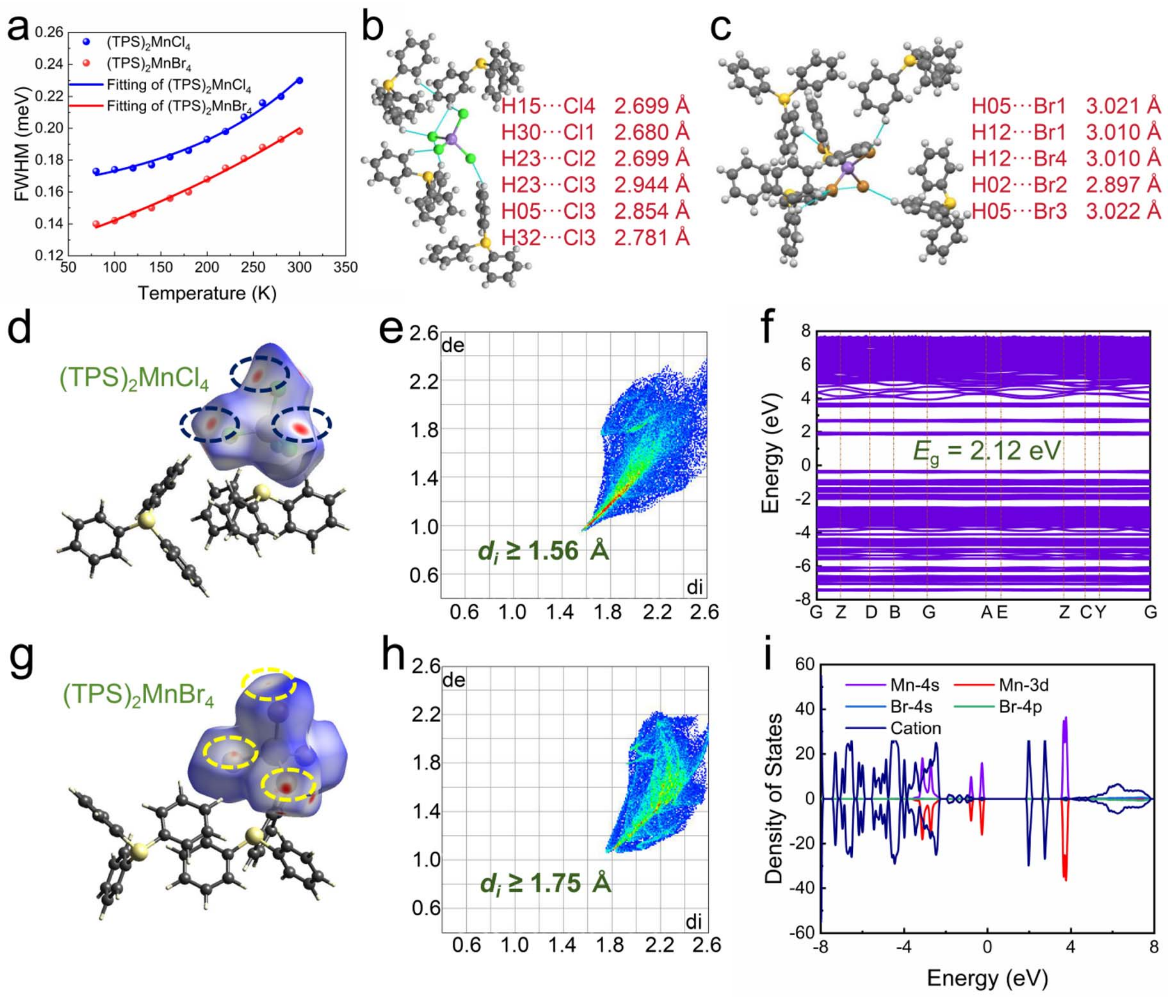

Fig. 3 (a) Temperature dependence of the emission FWHM (expressed in eV) for $(TPS)_2MnCl_4$ and $(TPS)_2MnBr_4$. Analysis of the estimated hydrogen bonding for crystals (b) (TPS)2MnCl$_4$ and (c) $(TPS)_2MnBr_4$. Hirshfeld surfaces for the (d) $[MnCl_4]^{2-}$ anion in $(TPS)_2MnCl_4$ and (g) $[MnBr_4]^{2-}$ anion in $(TPS)_2MnBr_4$, visualizing intermolecular close contacts (red indicating contacts shorter than van der Waals radii sum). Corresponding 2D fingerprint plots summarizing all intermolecular contacts for (e) $(TPS)_2MnCl_4$ and (h) $(TPS)_2MnBr_4$, plotting distance to d_i *vs.* d_e the surface. (f) Calculated electronic band structure along high-symmetry *k*-point paths for $(TPS)_2MnBr_4$, indicating a band gap of 2.12 eV. (i) Calculated total and partial DOS for $(TPS)_2MnBr_4$.

construction of highly saturated primary colors. As a result, the fabricated WLED achieved a wide color gamut covering 109% of the NTSC standard color space (Fig. 4c). This expansive gamut significantly surpasses what is typically achievable with broader green emitters and indicates the potential of $(TPS)_2MnBr_4$ for advanced liquid crystal display (LCD) backlighting requiring vibrant and lifelike colors. The device also exhibited good operational stability under varying electrical loads. When the driving current was increased from 20 mA to 120 mA, the EL spectral shape remained largely consistent ($\Delta\lambda = 0.8$ nm) (Fig. 4d), and the CIE 1931 chromaticity coordinates showed only minimal drift ($\Delta\text{CIE} = (0.1, 0.1)$) (Fig. 4e). Correspondingly, the CCT and CRI values also displayed good stability across this current range (Fig. 4b), indicating the robustness of the phosphor blend and packaging against increased operating power and associated thermal effects. Despite the overall performance of the $(TPS)_2MnBr_4$ being inferior to the recently reported copper halides,[42] it also provides a new pathway for high-performance halide WLEDs.

To evaluate the long-term reliability, the WLED device was subjected to continuous operation at a fixed voltage of 5.0 V. As shown in Fig. S15, the electroluminescence (EL) spectrum of the WLED was recorded at different time intervals up to 20 hours. The spectral shape and the relative intensities of the blue, green, and red emission peaks remain remarkably stable, indicating no significant degradation or color shift of the phosphor components during operation. In addition, the long-term lumen maintenance was tracked over 200 hours of continuous operation (Fig. S16). The device exhibits good durability, maintaining over 80% of its initial luminous efficacy (LE) after approximately 100 hours. The T50 lifetime (time to 50% of initial LE) is estimated to be approximately 175 hours. While further optimization of packaging is needed for commercial standards, this result demonstrates the

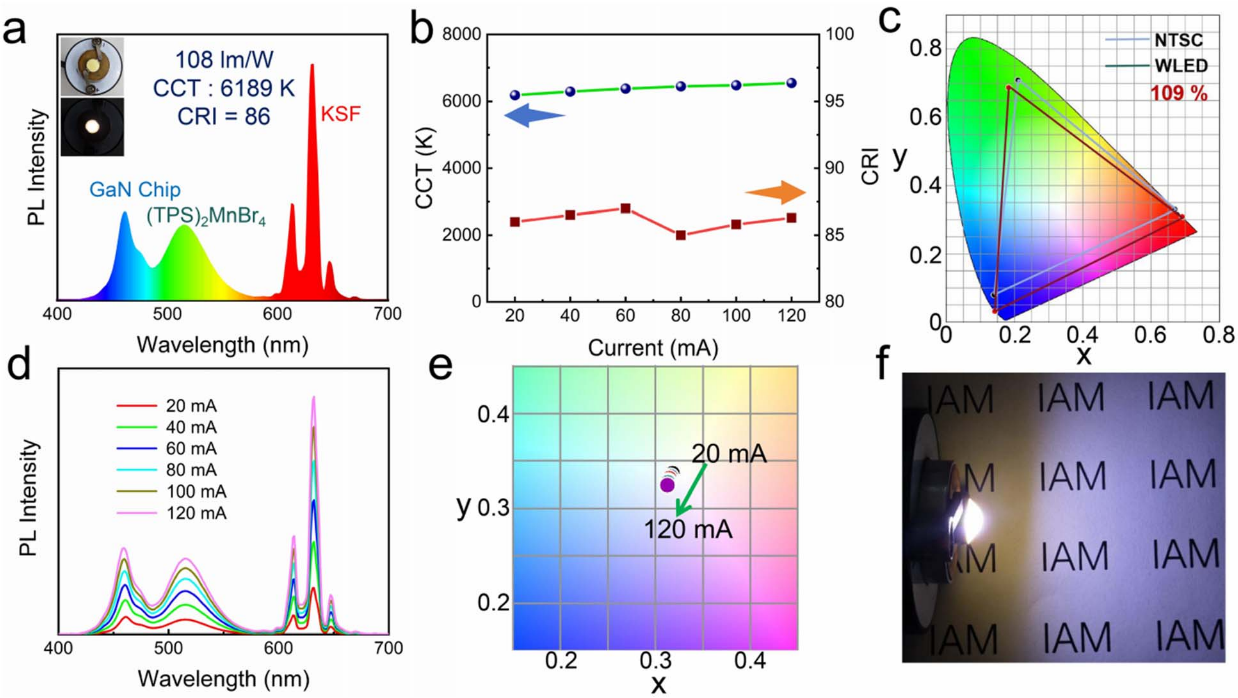

Fig. 4 (a) EL spectrum of the WLED (driven at 20 mA), composed of emission from the blue InGaN chip, green $(TPS)_2MnBr_4$, and red $K_2SiF_6:Mn^{4+}$ (KSF) phosphor. Insets show photographs of the packaged device off (top) and emitting white light (bottom). (b) Variation of the CRI and CCT of the WLED as a function of driving current (20–120 mA). (c) Color gamut of the WLED and the NTSC standard in CIE 1931 chromaticity coordinates. (d) EL spectra of the WLED recorded at various driving currents (20–120 mA). (e) CIE 1931 chromaticity coordinates of the WLED plotted for different driving currents (20–120 mA). (f) Photograph demonstrating the bright white light illumination produced by the fabricated WLED device.

fundamental stability of the $(TPS)_2MnBr_4$ phosphor under operational conditions. We also assessed the device's resilience to environmental factors, which is crucial for real-world applications. The WLED's luminous efficacy was measured after exposure to varying relative humidity (RH) levels (Fig. S17). The device maintains over 80% of its initial LE even at a harsh 100% RH, and notably shows excellent stability in the 40–60% RH range, demonstrating good moisture resistance. Also, the thermal quenching behavior of the packaged WLED was investigated by measuring its LE as a function of operating temperature, from 30 °C to 150 °C (Fig. S18). The device shows excellent thermal robustness, retaining approximately 70% of its initial efficacy even at a high temperature of 150 °C.

X-ray imaging application

Beyond its exceptional photoluminescence for WLEDs, the near-unity quantum efficiency of $(TPS)_2MnBr_4$ strongly suggested its potential as a high-performance scintillator for converting high-energy X-ray photons into detectable visible light. We therefore investigated its radioluminescence (RL) properties and imaging capabilities. Upon exposure to X-rays, both $(TPS)_2MnBr_4$ and $(TPS)_2MnCl_4$ exhibited green RL emission (Fig. 5a). The RL spectrum of $(TPS)_2MnBr_4$ peaked at 515 nm, perfectly matching its PL spectrum and confirming the emission originates from the $^4T_1(G) \rightarrow {}^6A_1(S)$ transition of the Mn^{2+} centers.[43] Notably, the integrated RL intensity of $(TPS)_2MnBr_4$ was significantly higher than that of $(TPS)_2MnCl_4$ and dramatically superior to a standard commercial $Bi_4Ge_3O_{12}$ (BGO) scintillator (Fig. S19) measured under identical conditions. Specifically, $(TPS)_2MnBr_4$ yielded an RL intensity 7.9 times greater than BGO. Assuming a light yield (LY) of ~10 000 photons per MeV for BGO,[44] this translates to an exceptionally high estimated LY of ~79 000 photons per MeV for $(TPS)_2MnBr_4$. Using commercial LuAG:Ce (22 000 photons per MeV) as the reference,[45] we determined that $(TPS)_2MnBr_4$ exhibits a light yield of approximately 78 000 photons per MeV (Fig. S20). Key performance metrics for dosimetry and detection were also evaluated. The RL intensity of $(TPS)_2MnBr_4$ demonstrated excellent linearity ($R^2 = 0.999$) with increasing X-ray dose rates across a wide range (0.15 to 3.35 μGy s^{-1}, Fig. 5b and c), which is crucial for accurate radiation measurement. Furthermore, a very low detection limit of 35.7 nGy s^{-1} was determined, highlighting its high sensitivity, which is nearly two orders of magnitude lower than typical dose rates used in medical diagnostics.[46]

To assess its potential for high-resolution imaging, a scintillator screen was fabricated from a $(TPS)_2MnBr_4$ wafer. Using the slanted-edge method, the spatial resolution was determined from the modulation transfer function (MTF) to be 18 lp mm^{-1} at MTF = 0.2 (Fig. S21 and. S22), indicating its capability for resolving fine details.[43,47] This was visually confirmed by successfully imaging the internal structure of an electronic chip, where features obscured in visible light were clearly

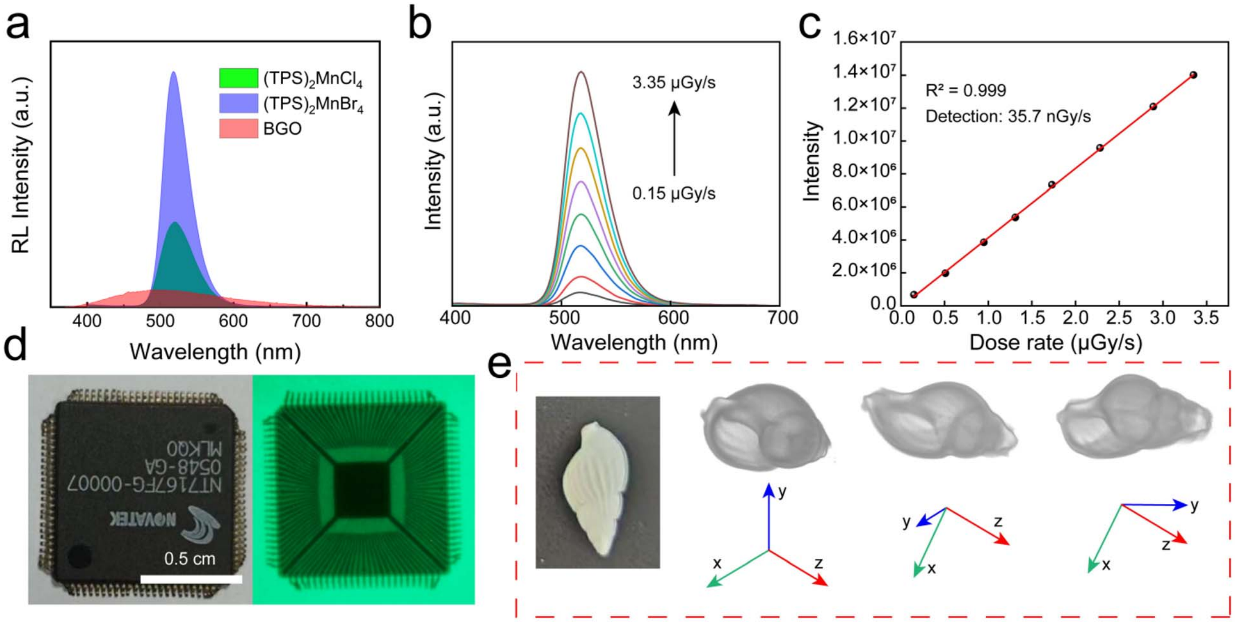

Fig. 5 (a) Comparison of RL spectra for $(TPS)_2MnCl_4$ (green shaded area), $(TPS)_2MnBr_4$ (blue shaded area), and a commercial BGO scintillator (red shaded area). (b) RL spectra of $(TPS)_2MnBr_4$ recorded under various X-ray dose rates (0.15 to 3.35 μGy s^{-1}). (c) Integrated RL intensity of $(TPS)_2MnBr_4$ as a function of X-ray dose rate. (d) X-ray radiograph of an electronic chip obtained using a scintillator screen fabricated from $(TPS)_2MnBr_4$. (e) Schematic diagram of the experimental setup used for X-ray imaging. (f) Demonstration of 3D X-ray imaging using the $(TPS)_2MnBr_4$ scintillator. Photograph of the conch sample (left) and selected views from the reconstructed 3D model (right) showing internal and external structures from different perspectives.

resolved under X-ray illumination using the $(TPS)_2MnBr_4$ screen (Fig. 5d). The radiation stability of the scintillators is shown in Fig. S23, under high-dose X-ray irradiation cycling, the radiation luminescence intensity of the $(TPS)_2MnBr_4$ remained stable, confirming its excellent radiation stability. Finally, we demonstrated the suitability of $(TPS)_2MnBr_4$ for advanced three-dimensional (3D) X-ray imaging reconstruction (Fig. S24). Using a customized setup (Fig. 5e), multiple 2D X-ray projection images of a conch shell were acquired at different rotation angles (5° intervals over 180°) using the $(TPS)_2MnBr_4$ scintillator screen. These projections were then processed using AVIZO software to reconstruct a high-fidelity 3D model of the conch (Fig. 5f, Video S1). The reconstructed images clearly reveal both the intricate internal structure and the external morphology of the shell from various viewing angles, showcasing the excellent performance of the $(TPS)_2MnBr_4$ scintillator for complex tomographic imaging tasks.

Conclusions

In conclusion, we have successfully designed and realized a novel, lead-free, 0D manganese(II) halide hybrid, $(TPS)_2MnBr_4$, which simultaneously achieves a near-unity PLQY ($\approx$99.6%) and a narrowed green emission band (FWHM = 40 nm). Through detailed structural and spectroscopic analysis, supported by theoretical calculations, we elucidated the crucial role of the rigid triphenylsulfonium cation. Its specific steric and electronic characteristics facilitate a crystal packing that minimizes distortion of the $[MnBr_4]^{2-}$ tetrahedra and promotes weaker cation–anion hydrogen bonding interactions compared to its chloride analogue. This structurally optimized environment leads directly to weaker electron–phonon coupling, fundamentally responsible for the observed narrow emission, while the effective isolation of emitters ensures the near-perfect quantum efficiency. The practical significance of achieving this synergy was demonstrated through the fabrication of high-performance devices for WLED and 3D X-ray imaging reconstruction. This work validates targeted cation engineering as a powerful strategy to overcome intrinsic performance limitations in Mn^{2+}-based emitters. It provides a clear design principle, correlating reduced structural distortion and weaker intermolecular interactions with suppressed electron–phonon coupling, for developing future high-performance, environmentally friendly manganese halide phosphors.

Author contributions

Y. Ma., and Q. Zhao. conceived the idea for this work and designed the experiments. M. Wang. contributed to the synthesis work, photophysical property study, measurements, and application study. X. Li., S. Zou., H. Cui., Y. Deng., J. Li., Y. Jiang contributed to implementation of the experiments. Y. Jiang., L. Wang., and S. Liu. revised the manuscript and provided suggestions. All authors discussed the results and commented on the manuscript at all stages.

Conflicts of interest

There are no conflicts to declare.

Data availability

CCDC 2364880 and 2364881 contain the supplementary crystallographic data for this paper.[49a,b]

The data supporting this article have been included as part of the Supplementary Information. Supplementary information is available. See DOI: **https://doi.org/10.1039/d5sc04721h**.

Acknowledgements

We gratefully acknowledge the financial support from National Natural Science Foundation of China (62322508, 62288102 and 62075101), Funded by Basic Research Program of Jiangsu (BK20243057), Jiangsu Funding Program for Excellent Postdoctoral Talent (2024ZB087 and 2024ZB133), the Postdoctoral Fellowship Program of CPSF (GZC20240744), China Postdoctoral Science Foundation (2024M761489 and 2024M751502).

Notes and references

1 Y. Deng, Y. Zhu, X. Zhao, N. Ding, Y. Yang, M. Wang, J. Li, P. She, S. Liu, Y. Ma and Q. Zhao, *Angew. Chem., Int. Ed.*, 2025, **64**, e202514416.

2 S. Wang, H. Lian, Y. Yang, Z. Wu, Y. Li, H. Ling, W. Pisula, T. Marszalek and T. Xu, *FlexMat*, 2025, **2**, 82–106.

3 Y. Zhu, X. Liang, X. Zhao, H. Cui, A. Yu, K. Y. Zhang, S. Liu, F. Wang and Q. Zhao, *Laser Photonics Rev.*, 2025, **19**, 2401802.

4 X. Cheng, Z. Dou, H. Lian, Z. Qin, H. Guo, X. Li, W. Wong and Q. Dong, *FlexMat*, 2024, **1**, 127–149.

5 B. Li, K. Han, Y. Wang, Y. Sun, Z. Xia and Y. Xu, *Angew. Chem., Int. Ed.*, 2025, **64**, e202502440.

6 Z. Zhou, Y. Xue, R. Hu, G. Yan, Y. Deng, S. Liu, F. Wang and Q. Zhao, *Laser Photonics Rev.*, 2025, **19**, 2500657.

7 Dinesh and A. Sharma, *Ceram. Int.*, 2025, **51**, 31359–31369.

8 J. Lu, J. Gao, S. Wang, M. Xie, B. Li, W. Wang, J. Mi, F. Zheng and G.-C. Guo, *Nano Lett.*, 2023, **23**, 4351–4358.

9 X. Zhao, M. Wu, H. Liu, Y. Wang, K. Wang, X. Yang and Bo Zou, *Adv. Funct. Mater.*, 2022, **32**, 2109277.

10 K. Han, K. Sakhatskyi, J. Jin, Q. Zhang, M. V. Kovalenko and Z. Xia, *Adv. Mater.*, 2022, **34**, 2110420.

11 J. Zhao, T. Zhang, X. Dong, M. Sun, C. Zhang, X. Li, Y. Zhao and S. Zang, *J. Am. Chem. Soc.*, 2019, **141**, 15755–15760.

12 L. Mao, P. Guo, S. Wang, A. K. Cheetham and R. Seshadri, *J. Am. Chem. Soc.*, 2020, **142**, 13582–13589.

13 L. Xu, X. Lin, Q. He, M. Worku and B. Ma, *Nat. Commun.*, 2020, **11**, 4329.

14 J. Li, C. Wang, H. Wu, L. Liu, Q. Xu, S. Ye, L. Tong, X. Chen, Q. Gao, Y. Hou, F. Wang, J. Tang, L. Chen and Y. Zhang, *Adv. Funct. Mater.*, 2021, **31**, 2102848.

15 H. Peng, T. Huang, B. Zou, Y. Tian, X. Wang, Y. Guo, T. Dong, Z. Yu, C. Ding, F. Yang and J. Wang, *Nano Energy*, 2021, **87**, 106166.

16 M. Wang, X. Wang, B. Zhang, F. Li, H. Meng, S. Liu and Q. Zhao, *J. Mater. Chem. C*, 2023, **11**, 3206–3212.

17 X. Wang, X. Zhang, Y. Liu and Y. Zhang, *Chem. Eng. J.*, 2024, **483**, 149239.

18 L. Gong, Q. Hu, F. Huang, Z. Zhang, N. Shen, B. Hu, Y. Song, Z. Wang, K. Du and X. Huang, *Chem. Commun.*, 2019, **55**, 7303–7306.

19 X. Jiang, S. Xia, J. Zhang, D. Ju, Y. Liu, X. Hu, L. Wang, Z. Chen and X. Tao, *ChemSusChem*, 2019, **12**, 5228–5232.

20 J. Zhang, X. Wang, W. Wang, X. Deng, C. Yue, X. Lei and Z. Gong, *Inorg. Chem.*, 2024, **63**, 26472654.

21 Y. Guo, J. Wu, W. Liu and S. Guo, *Inorg. Chem.*, 2022, **61**, 11514–11518.

22 V. Morad, I. Cherniukh, L. Pöttschacher, Y. Shynkarenko, S. Yakunin and M. V. Kovalenko, *Chem. Mater.*, 2019, **31**, 10161–10169.

23 J. Chen, J. Luo, Z. He, Q. Peng, J. Wei, Z. Zhang, X. Guo and D. Kuang, *Chem. Sci.*, 2025, **16**, 9375–9384.

24 W. Huang, Y. Chen, Y. Lin, A. Lazarowska, N. Majewska, S. Mahlik, G. Leniec, H. Huang, A. Singh, D. Huang, P. Fu, Z. Xiao and R. Liu, *Small*, 2025, **21**, 2501075.

25 Y. Wu, Y. Zhu, A. A. Ahmed, M. Imran, S. Qiu, Y. Liu, X. Hu, Y. Hassan, Z. Sun, R. Deng and X. Li, *Angew. Chem., Int. Ed.*, 2025, **64**, e202417018.

26 G. Dong, B. Hu, C. Chen, H. Yu, Q. Han and W. Wu, *Inorg. Chem.*, 2024, **63**, 20830–20839.

27 A. B. Abdelhadi, M. Gutiérrez, B. Cohen, L. Lezama, M. Lachkar and A. Douhal, *J. Mater. Chem. C*, 2024, **12**, 286–295.

28 T. Chang, Y. Dai, Q. Wei, X. Xu, S. Cao, B. Zou, Q. Zhang and R. Zeng, *ACS Appl. Mater. Interfaces*, 2023, **15**, 5487–5494.

29 L. Mao, J. Chen, P. Vishnoi and A. K. Cheetham, *Acc. Mater. Res.*, 2022, **3**, 439–448.

30 S. Zhang, Y. Zhao, J. Zhou, H. Ming, C. Wang, X. Jing, S. Ye and Q. Zhang, *Chem. Eng. J.*, 2021, **421**, 129886.

31 G. Zhou, Z. Liu, J. Huang, M. S. Molokeev, Z. Xiao, C. Ma and Z. Xia, *J. Phys. Chem. Lett.*, 2020, **11**, 5956–5962.

32 J. Lin, M. Zhang, N. Sun, S. He, X. Zhang, Z. Guo, J. Zhao, Q. Liu and W. Yuan, *J. Mater. Chem. C*, 2022, **10**, 16773–16780.

33 M. Lun, H. Ni, Z. Zhang, J. Li, Q. Jia, Y. Zhang, Y. Zhang and D. Fu, *Angew. Chem., Int. Ed.*, 2024, **63**, e202313590.

34 J. Liao, Z. Zhang, G. Wang, L. Zhou, N. Yi, Z. Tang and G. Xing, *Angew. Chem., Int. Ed.*, 2024, **63**, e202419085.

35 R. Zhang, H. Xie, W. Liu, K. Zhan, H. Liu, Z. Tang and C. Yang, *ACS Appl. Mater. Interfaces*, 2023, **15**, 47238–47249.

36 H. Liu, H. Ru, M. Sun, Z. Wang and S. Zang, *Adv. Opt. Mater.*, 2022, **18**, 2101700.

37 L. Y. Lian, W. Qi, H. Y. Ding, H. Tian, Q. Ye, Y. B. Zhao, L. Zhao, J. B. Gao, D. L. Zhang and J. B. Zhang, *Nano Res.*, 2022, **15**, 8486–8492.

38 S. D. Stranks, V. M. Burlakov, T. Leijtens, J. M. Ball, A. Goriely and H. J. Snaith, *Phys. Rev. Appl.*, 2014, **2**, 034007.

39 J. Chatterjee, R. Tanwar, S. Anupama, A. Chatterjee, M. D. Ambhore, M. Kabir, P. Mandal and P. Hazra, *J. Phys. Chem. Lett.*, 2025, **16**, 1549–1558.

40 K. Robinson, G. V. Gibbs and P. H. Ribbe, *Science*, 1971, **172**, 567–570.

41 Y. Fan, P. Wang, C. Chen, X. Ji, F. Chang and L. Mao, *Sci. China. Chem.*, 2025, **68**, 4160–4171.

42 Y. Chen, H. Zhu, D. Babaian, C. Dzorkpata, A. Grigoriev, Z. Wang, S. Wheat, S. Guha and P. Zhu, *Adv. Mater.*, 2025, **37**, 2500083.

43 H. Meng, W. Zhu, Z. Zhou, R. Zhou, D. Yan, Q. Zhao and S. Liu, *J. Mater. Chem. C*, 2022, **10**, 12286–12291.

44 H. Cui, Y. Yan, Z. Feng, Y. Zhu, Y. Feng, S. Liu and Q. Zhao, *Laser Photonics Rev.*, 2025, **19**, 2401321.

45 Z. Feng, H. Cui, Y. Yan, S. Liu and Q. Zhao, *Laser Photonics Rev.*, 2025, **19**, e00885.

46 J. Chen, J. Luo, Q. Peng, Z. He, J. Wei and D. Kuang, *Angew. Chem., Int. Ed.*, 2025, **64**, e202508536.

47 J. Su, J. Wei, K. Ye, F. Li, M. Wang, Q. Li, A. Yuan, Q. Zhao and C. Shi, *Chem. Commun.*, 2025, **61**, 5475–5478.

48 Deposition number 2364880 (for $(TPS)_2MnBr_4$) and 2364881 (for $(TPS)_2MnCl_4$) contains the supplementary crystallographic data for this paper. These data are provided free of charge by the joint Cambridge Crystallographic Data Centre and Fachinformationszentrum Karlsruhe Access Structures service.

49 (*a*) CCDC 2364880: Experimental Crystal Structure Determination, 2025, DOI: **10.5517/ccdc.csd.cc2kcvg8**; (*b*) CCDC 2364881: Experimental Crystal Structure Determination, 2025, DOI: **10.5517/ccdc.csd.cc2kcvh9**.